

# Probing confinement in a $\mathbb{Z}_2$ lattice gauge theory on a quantum computer

Julius Mildenberger,<sup>1,\*</sup> Wojciech Mruczkiewicz,<sup>2</sup> Jad C. Halimeh,<sup>1,3,4</sup> Zhang Jiang,<sup>2</sup> and Philipp Hauke<sup>1,†</sup>

<sup>1</sup>*INO-CNR BEC Center and Department of Physics,  
University of Trento, Via Sommarive 14, I-38123 Trento, Italy*

<sup>2</sup>*Google Quantum AI, Venice, California, USA*

<sup>3</sup>*Department of Physics and Arnold Sommerfeld Center for Theoretical Physics (ASC),  
Ludwig-Maximilians-Universität München, Theresienstraße 37, D-80333 München, Germany*

<sup>4</sup>*Munich Center for Quantum Science and Technology (MCQST), Schellingstraße 4, D-80799 München, Germany*

(Dated: August 30, 2022)

Digital quantum simulators provide a tabletop platform for addressing salient questions in particle and condensed-matter physics. A particularly rewarding target is given by lattice gauge theories (LGTs) [1, 2]. Their constituents, e.g., charged matter and the electric gauge field, are governed by local gauge constraints, which are highly challenging to engineer and which lead to intriguing yet not fully understood features such as confinement of particles [3, 4]. Here, we simulate confinement dynamics in a  $\mathbb{Z}_2$  LGT on a superconducting quantum chip. We synthesize the charge–gauge-field interaction using only 6 native two-qubit gates, enabling us to reach simulation times of up to 25 Trotter steps. We observe how tuning a term that couples only to the electric field confines the charges, a manifestation of the tight bond that the local gauge constraint generates between both. Moreover, we study a different mechanism, where a modification of the gauge constraint from a  $\mathbb{Z}_2$  to a U(1) symmetry freezes the system dynamics. Our work showcases the dramatic restriction that the underlying gauge constraint imposes on the dynamics of an LGT, it illustrates how gauge constraints can be modified and protected, and it paves the way for studying other models governed by many-body interactions.

The rich phenomenology of gauge theories is fundamentally linked with local constraints set by the underlying gauge symmetry, which determine the interplay between matter and gauge degrees of freedom. For example, the non-Abelian gauge symmetry of quantum chromodynamics confines quarks together with gluons into hadrons due to their mutual interaction, and quantum electrodynamics (QED) hosts a local U(1) symmetry, the well-known Gauss’s law, that is responsible for the massless photon and the emergence of the long-ranged Coulomb law [3, 4]. Originally employed to address nonperturbative regimes in particle physics [3], lattice discretizations of gauge theories have proven to be powerful frameworks to describe the emergence of exotic phenomena also in

condensed-matter physics including, e.g., disorder-free localization [5], quantum many-body scars [6], and staircase prethermalization [7].

Among the most fascinating phenomena in LGTs is confinement, by which the system dynamics is restricted due to interactions that are mediated via the gauge field. Confinement can give rise to bound meson excitations and in some cases is even associated with topological phases with non-Abelian anyons and charge fractionalization [4]. In the presence of both dynamical matter and gauge fields, the confinement problem is not fully understood, due to the difficulty of solving general LGTs using classical methods [3, 8].

In recent years, there is emerging an alternative computing paradigm, quantum simulation, which uses quantum rather than classical hardware to solve quantum many-body problems. Though in principle universal quantum computers can perform fully scalable quantum simulations, the current devices are still of limited size and coherence times [2, 9]. This state of affairs makes LGTs particularly appealing target models for quantum simulation: Not only do they host extremely rich physics, the gauge symmetry also presents a new handle on hardware errors as a diagnostic tool and by stimulating the design of new error-mitigation schemes [10–13].

Here, we experimentally probe confinement in a LGT with  $\mathbb{Z}_2$  gauge symmetry (Fig. 1a) using up to 21 qubits in a superconducting quantum chip. We realize the dynamics of the LGT using Trotterization to discretize time and compose the system Hamiltonian through elementary gates (Fig. 1b). The most challenging term, and the heart of our algorithm, is the interaction process between charged matter and gauge fields, which we synthesize as a gauge-invariant three-qubit gate using only 6 native two-qubit gates (Fig. 1c). This enables us to simulate the dynamics up to 25 Trotter steps, equivalent to a two-qubit gate depth of up to 202. In a further experiment, we add the local generators associated with a U(1) LGT to the model Hamiltonian, permitting us to controllably tune the system from a local  $\mathbb{Z}_2$  to a U(1) gauge symmetry. As we show, the modification of the underlying gauge symmetry can dramatically restrain the charge dynamics.

Our work adds an important piece to the puzzle of quantum simulations of LGTs with coupled matter and gauge fields. At the moment, most existing realiza-

\* [julius.mildenberger@unitn.it](mailto:julius.mildenberger@unitn.it)

† [philipp.hauke@unitn.it](mailto:philipp.hauke@unitn.it)

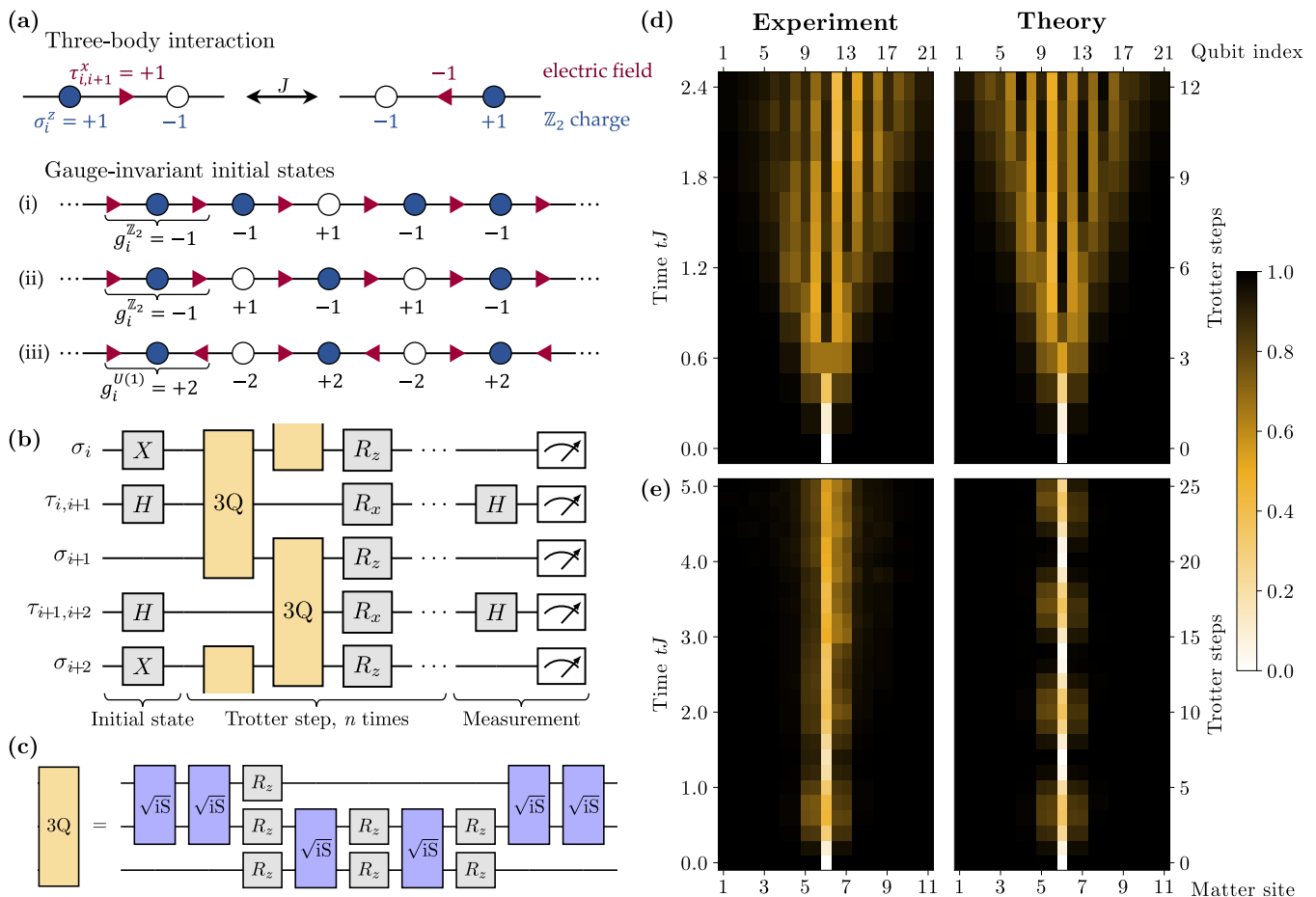


Figure 1. **Simulating confinement in a  $\mathbb{Z}_2$  lattice gauge theory on a digital superconducting chip.** (a) Target gauge theory. Charged matter (Pauli operators  $\sigma_i$ ) lives on sites  $i$  and gauge fields (Pauli operators  $\tau_{i,i+1}$ ) on links. The dynamics of charges and gauge field is coupled by a three-qubit (3Q) interaction term  $H_J$  and constrained by a  $\mathbb{Z}_2$  gauge symmetry, embodied in the conservation of the local generators  $G_i^{\mathbb{Z}_2} = -\tau_{i-1,i}^x \sigma_i^z \tau_{i,i+1}^x$ . Our simulations use three different types of gauge-invariant initial states. (b) Circuit. The dynamics is implemented by Trotterizing the Hamiltonian into gauge–matter interaction  $H_J$ , the matter rest mass (realized by  $z$ -rotations) and a background electric field ( $x$ -rotations), for a total circuit depth of 8 two-qubit layers per Trotter step. Some of our experiments add a term that protects a U(1) gauge symmetry by single-qubit rotations, permitting us to tune the system between a  $\mathbb{Z}_2$  and U(1) gauge theory. These can be incorporated into the single-qubit  $x/z$ -rotations already employed to implement the matter rest mass and background electric field, thereby not increasing gate depth. (c) Three-qubit matter–gauge–field interaction. The experiment is enabled by synthesizing the three-qubit interaction in a fully gauge-invariant manner using only 6 two-qubit gates and 3 layers of single-qubit gates. As  $z$ -rotations, the latter do not require execution time (Methods). (d,e) Confinement dynamics. Plotted is the inverse excitation of qubits, which for odd qubit numbers gives  $(\mathbb{1} + \sigma_i^z)/2$ , corresponding to the  $\mathbb{Z}_2$  charge  $-\sigma_i^z$ , and on even qubit numbers  $(\mathbb{1} + \tau_{i,i+1}^x)/2$  corresponding to the electric field  $\tau_{i,i+1}^x$ . At small background field strength  $f$ , a matter defect can spread over the entire system (d), while with increasing  $f$  it is confined, purely due to the interaction with the gauge field (e). Theory predictions agree well with the experimental data from the superconducting Sycamore-class chip.

tions concern continuous gauge groups [13–18]. Pioneering laboratory demonstrations for a discrete  $\mathbb{Z}_2$  gauge symmetry considered building-blocks [19] and perturbative implementations [20]. Here, we develop a non-perturbative, fully gauge-invariant decomposition, enabling us to demonstrate confinement in a few tens of qubits, to probe long evolution times, and to add an experimentally simple term that tunes the underlying gauge symmetry. Our experiments thus open the door towards controlling gauge symmetries in digital quantum simula-

tions and studying the rich dynamics of matter coupled to gauge fields with discrete gauge symmetry.

**Target theory.**—We are interested here in Abelian LGTs, as sketched in Fig. 1a. Charged matter lives on sites  $i = 0, \dots, N-1$  of a one-dimensional spatial lattice. Following a Jordan–Wigner transformation (see Methods), we denote the associated operators by Pauli matrices  $\sigma_i$ . The electric field lives on links between sites, with associated Pauli matrices  $\tau_{i,i+1}^x$ . The target LGT is

governed by the Hamiltonian  $H = H_J + H_f + H_m$ , with

$$H_J = J \sum_i (\sigma_i^+ \tau_{i,i+1}^z \sigma_{i+1}^- + \text{h.c.}), \quad (1a)$$

$$H_f = f \sum_i \tau_{i,i+1}^x, \quad (1b)$$

$$H_m = \frac{\mu}{2} \sum_i (-1)^i \sigma_i^z. \quad (1c)$$

Here,  $H_m$  describes the rest mass of matter and  $H_f$  is a background field term. This term generates a confining potential for the charges: when  $f = 0$ , the theory is deconfined while charges are confined at  $f \neq 0$  [19]. The most challenging part of the implementation is the three-qubit term  $H_J$ , which couples matter and gauge fields.

The essence of a LGT is the conservation of a local symmetry. For the case of Hamiltonian  $H$ , this is a  $\mathbb{Z}_2$  gauge symmetry. It is embodied in the conservation of  $G_i^{\mathbb{Z}_2} = -\tau_{i-1,i}^x \sigma_i^z \tau_{i,i+1}^x$ , i.e.,  $[H, G_i^{\mathbb{Z}_2}] = 0, \forall i$ . Further below, we will demonstrate how an energy penalty term [10] tunes the  $\mathbb{Z}_2$  to an approximate U(1) gauge symmetry, such as governs QED. The associated symmetry generator is  $G_i^{U(1)} = \frac{1}{2} [\tau_{i-1,i}^x - \tau_{i,i+1}^x + \sigma_i^z + (-1)^i]$ , corresponding to a lattice version of Gauss's law. It is these local gauge symmetries that are responsible for the richness of fundamental phenomena in LGTs. Conserving these local symmetries for all simulated times  $t$  is the central challenge of gauge-theory quantum simulation.

**Hardware implementation.**—In our implementation, we synthesize the target time-evolution operator generated by  $H$  through a first-order Trotter–Suzuki decomposition,

$$U(t) = e^{-iHt} \simeq \left( \prod_{\ell} e^{-iH_{\ell}\Delta t} \right)^n, \quad (2)$$

with  $n$  the number of Trotter steps,  $\Delta t = t/n$  the Trotter time step, and  $H_{\ell} \in \{H_m, H_f, H_J\}$ . Taking advantage of a recently elucidated chaos-regular transition in Trotterized dynamics [21, 22], we can work faithfully at large Trotter steps of  $\Delta t \in \{0.2/J, 0.3/J\}$ , and thus reach considerable simulated times within accessible laboratory decoherence times (Methods).

We experimentally implement the  $\mathbb{Z}_2$  LGT on up to 21 gmon qubits of a superconducting quantum processor of the Sycamore class (Methods). This chip natively supports single-qubit  $z$ -rotations, rotations along arbitrary axes on the  $x$ - $y$  plane, and two-qubit gates that are close to  $\sqrt{\text{iSWAP}}^{\dagger} = \exp(-i\frac{\pi}{8}(\sigma_1^x \sigma_2^x + \sigma_1^y \sigma_2^y))$ . The major implementational challenge is given by the multi-qubit gates constituting  $H_J$ . For these, we have designed an efficient realization using 6  $\sqrt{\text{iSWAP}}^{\dagger}$  gates and 3 layers of single-qubit  $z$ -rotations (Fig. 1c), the latter of which do not require execution time (Methods). To put this into context, the best existing decomposition of arbitrary three-qubit circuits requires up to 20 CNOT gates [23]. By parallelizing gates acting on neighboring triples, a single Trotter step can be compressed to a depth of 8  $\sqrt{\text{iSWAP}}^{\dagger}$  gates

instead of the 12 one might naively expect (Methods). The respective initial state (Fig. 1a) is prepared from the fiducial state  $|0\rangle^{\otimes L}$ , with  $L$  being the number of qubits, using single-qubit rotations. Compressing the depth of the circuit, altogether a single Trotter step takes 256ns enabling coherent experiments up to 25 Trotter steps for a total run time of an experimental shot up to 6.5 $\mu$ s, including state preparation and basis rotations for measurement. After the desired number of Trotter steps, we measure the qubits in the computational basis (averaging over 50000 to 200000 shots for each configuration). These measurements hand us a wide range of observables, including matter density, electric-field strength, and degree of violation of U(1) and  $\mathbb{Z}_2$  gauge invariance. To increase the data quality (Methods), we employ Floquet calibration and average over 5-10 different qubit configurations on the chip. Further, device errors that violate conservation of total matter charge as well as the  $\mathbb{Z}_2$  Gauss's law are mitigated by postselecting on these ideally conserved quantities, which is possible thanks to single-site readout.

**Confinement in a  $\mathbb{Z}_2$  LGT.**—As a first probe of confinement in the target LGT, we initialize the system in the state of Fig. 1a(i). This state contains a matter defect at the central site and a fully polarized electric field. We quench the system with  $H$ , with  $\Delta t = 0.2/J$ ,  $\mu = 0$ , and  $f \in \{0.2J, 2.0J\}$ , and track in the subsequent dynamics the position of the defect as well as the electric-field excitation through the local  $\mathbb{Z}_2$  charge  $-\sigma_i^z$  and  $\tau_{i,i+1}^x$ , respectively.

As the experimental data in Fig. 1d,e show, for a low value of  $f = 0.2J$  the action of the term  $H_J$  quickly spreads the charge defect. Enforced by gauge invariance, the charge's motion changes correspondingly the expectation value of the electric field  $E_{i,i+1} = \tau_{i,i+1}^x$ . Upon increasing  $f$ , the defect remains confined to a narrow region, even up to evolution times considerably larger than the scale of  $H_J$ . The experimental data agrees well with theory. The main differences are attributable to parasitic C-phase gates appearing with the  $\sqrt{\text{iSWAP}}^{\dagger}$  gates (see Fig. 3 and Methods). A small spatial asymmetry arises from the Trotterization of  $H_J$  where  $\sigma_i^+ \tau_{i,i+1}^z \sigma_{i+1}^- + \text{h.c.}$  and  $\sigma_{i+1}^+ \tau_{i+1,i+2}^z \sigma_{i+2}^- + \text{h.c.}$  are applied subsequently (see Fig. 1b). Remarkably, the parameter that is tuned in this experiment couples only to the gauge field, demonstrating how charge confinement appears purely as a consequence of coupling between matter and gauge fields.

To further probe confinement, we initialize the system at half matter filling in the state of Fig. 1a(ii). Figure 2a displays the dynamics of the average electric field

$$\mathcal{E}(t) = \frac{1}{N} \sum_i \langle \tau_{i,i+1}^x(t) \rangle \quad (3)$$

for eight matter sites under periodic boundary conditions plus the eight associated gauge fields. Initially, the field is fully polarized. Due to the matter–gauge-field coupling  $H_J$ , each matter-hopping event flips the electric field in

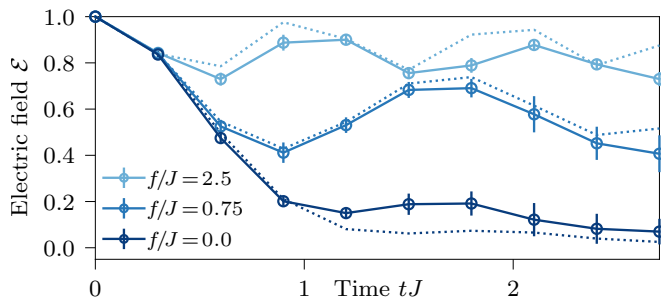


Figure 2. **Confinement in a  $\mathbb{Z}_2$  gauge theory of 16 qubits.** For small strengths of the background field term  $f$ , charges move through the system and thus flip the electric fields, whose average  $\mathcal{E}$  relaxes to 0 (dark curve). As  $f$  is increased (lighter curves), the system becomes gradually more confined, preventing a full relaxation of  $\mathcal{E}$ . Experimental data (symbols connected by solid line) agrees well with ideal theory predictions (dotted line). Statistical errors bars denote one standard deviation over 10 different circuit layouts. Data for 8 matter sites plus 8 gauge fields with periodic boundary conditions,  $\mu = 0.35J$ .

between the involved sites. Thus, under deconfined dynamics the average electric field eventually vanishes. In contrast, as  $f$  is increased, the charges become confined [19], and the electric field remains close to its initial configuration.

**Confinement by modifying the gauge constraint.**—Finally, we demonstrate an entirely different mechanism for confinement, where not a tuning of the model parameters but a modification of the underlying gauge symmetry drastically restrains the dynamics.

Consider the apparently simple modification of the gauge-matter coupling from Eq. (1a) to

$$H_J^{\text{U}(1)} = J \sum_i [\sigma_i^+ (\tau_{i,i+1}^z - i\tau_{i,i+1}^y) \sigma_{i+1}^- + \text{h.c.}] \quad (4)$$

(the term in round brackets corresponds to a spin-raising operator in the  $x$  direction of the Bloch sphere). The Hamiltonian  $H^{\text{U}(1)} = H_J^{\text{U}(1)} + H_f + H_m$  has acquired a U(1) gauge symmetry, i.e.,  $[H^{\text{U}(1)}, G_i^{\text{U}(1)}] = 0, \forall i$ . Now consider the initial state in Fig. 1a(iii), denoted as  $|\psi_3\rangle$ . This state is consistent with both  $\mathbb{Z}_2$  and U(1) gauge symmetry, with eigenvalues  $G_i^{\mathbb{Z}_2} |\psi_3\rangle = (-1)^i |\psi_3\rangle$  and  $G_i^{\text{U}(1)} |\psi_3\rangle = 2(-1)^i |\psi_3\rangle$ . If evolved under  $H$ , only the  $\mathbb{Z}_2$  gauge symmetry will be preserved. Moreover, the charges can move by flipping the gauge fields on the involved links. In contrast, if  $|\psi_3\rangle$  is evolved under  $H^{\text{U}(1)}$ , not only is the U(1) gauge symmetry preserved, but also the charges are blocked: there are no gauge fields that the action of  $H_J^{\text{U}(1)}$  could flip.

To demonstrate this phenomenon, we generate an effective U(1) gauge symmetry by adding terms proportional to its gauge generators  $G_i^{\text{U}(1)}$  [10]. Similar symmetry-protecting schemes have been used in the lab-

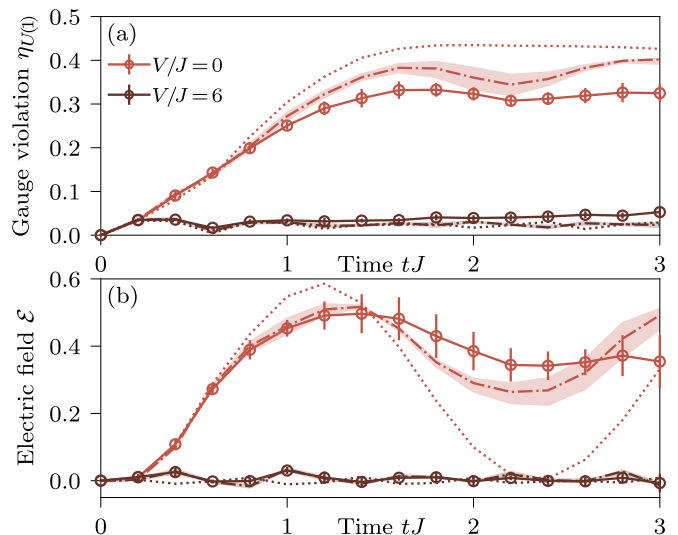


Figure 3. **Gauge protection and confinement induced by modifying the local conservation law.** (a) The dynamics under the  $\mathbb{Z}_2$  gauge theory  $H$  quickly violates the U(1) gauge symmetry of the initial state given in Fig. 1a(iii) ( $V/J = 0$ , light). Adding a penalty term  $H_G$  efficiently suppresses U(1) gauge violations even for rather moderate protection strengths of  $V/J = 6$  (dark) and controllably tunes the  $\mathbb{Z}_2$  into a U(1) gauge symmetry. (b) The dynamics of the electric field depend drastically on the local conservation law that governs the system. In the original  $\mathbb{Z}_2$  theory,  $\mathcal{E}(t)$  rises quickly to large values. In stark contrast, in presence of a gauge protection term the emerging local U(1) symmetry prevents any charges from hopping—the system becomes confined, solely by modifying its local conservation laws. Numerical simulations that take the parasitic C-phase (Methods) into account (dashed lines and shaded region) explain well the leading deviations between experiment (symbols connected by solid line) and the ideal theory (dotted line). Data for 6 matter plus 6 gauge fields (12 qubits) with periodic boundary conditions,  $f = \mu = 2.5J$ , statistical errors bars denote one standard deviation over 10 different circuit layouts.

oratory to perturbatively realize LGTs [13, 17, 20]. Here, we employ these to tune from the original  $\mathbb{Z}_2$  to a U(1) theory.

Importantly, the employed term  $H_G = V \sum_i c_i G_i^{\text{U}(1)}$  consists of only single qubit operations, which can be absorbed into those already present to implement  $H_f$  and  $H_m$  (Methods). While  $H_G$  commutes with the mass and background-field terms, it does compete with the gauge-matter coupling  $H_J$ . Illustratively, one can imagine  $H_G$  to rapidly rotate the  $\mathbb{Z}_2$  gauge field operator  $\tau_{i,i+1}^z$  around the  $x$ -axis [10–12]. In a time-averaged fashion,  $H_J$  thus effectively acquires the U(1) symmetry of a circle in the  $z$ - $y$  plane. At large  $V/J$ , one thus approximately obtains  $H^{\text{U}(1)}$  [10]. Remarkably, we find small values of  $V/J = 6$  are already sufficient for observing striking effects.

Initializing the system in  $|\psi_3\rangle$  and quenching with the  $\mathbb{Z}_2$  theory  $H$  alone quickly leads to violation of the U(1)



gauge symmetry, quantified through

$$\eta_{U(1)} = \frac{1}{\kappa N} \sum_i \left\langle \left( G_i^{U(1)} + 2(-1)^i \right)^2 \right\rangle, \quad (5)$$

(light curves in Fig. 3a), where  $\kappa = 9$  normalizes the theoretical maximum of the gauge violation to unity. In contrast, by adding a moderately strong protection term  $H_G$ , the  $U(1)$  gauge violation is suppressed to small values throughout the entire evolution time (dark curves).

This modification of the underlying gauge symmetry has dramatic repercussions on the entire system dynamics: In the  $\mathbb{Z}_2$  theory (small  $V/J$ ), the charges are free to move and we observe a strong dynamics also in the electric field (light curves in Fig. 3b). Instead, upon tuning the symmetry towards  $U(1)$  by means of  $H_G$ , charges stay confined and the electric field remains close to its initial value for the entire evolution time.

**Outlook.**—Our work opens the door to studying a wide range of phenomena in LGTs of coupled matter and gauge fields with discrete symmetries. Ideal target scenarios are, e.g., exotic out-of-equilibrium phenomena such as quantum many-body scars [6] and disorder-free localization [5]. Given the large computational challenges when attempting to connect early-time behavior to late-time dynamics, thermalization of gauge theories is another outstanding question with large relevance, e.g., to high-energy experiments such as heavy-ion collisions [8].

The necessity of precisely engineering multi-qubit interactions and local constraints is currently imparting a strong momentum onto the field, as it pushes devices beyond their current limits and drives the development of new error mitigation protocols [11–13, 17, 20], such as the

one implemented here [10]. Promising proposals exist for generalizing such schemes to more complex situations, including non-Abelian gauge theories [11, 12, 24].

Such investigations may also develop interesting cross-fertilizations to other fields. E.g., postselecting on the Gauss’ law is similar to syndrome measurements in error-correcting codes [25]. Beyond the immediate context of LGTs, three-body gates as designed here are a key ingredient for manifold physical scenarios, including cluster Ising models [26], topological phase transitions [27], spin chirality [28], multipartite entanglement [28], and even non-stoquastic and parity quantum annealing [29].

**Acknowledgements.**—We are grateful to the Google Quantum AI team, in particular Eric Ostby and Markus Hoffmann, for support and discussions. We also thank Haifeng Lang for discussions. We acknowledge participation in the Google Quantum AI Early Access Program, within which all quantum computations have been performed between two continents via the cloud, employing the high-level language Cirq. This work is supported by the ERC Starting Grant StrEnQTh (project ID 804305), the Google Research Scholar Award ProGauge, Provincia Autonoma di Trento, and by Q@TN, the joint lab between University of Trento, FBK-Fondazione Bruno Kessler, INFN-National Institute for Nuclear Physics and CNR-National Research Council. This project has received funding from the European Research Council (ERC) under the European Union’s Horizon 2020 research and innovation program (Grant Agreement no 948141) — ERC Starting Grant SimUcQuam, and by the Deutsche Forschungsgemeinschaft (DFG, German Research Foundation) under Germany’s Excellence Strategy – EXC-2111 – 390814868.

- 
- [1] M. C. Bañuls, R. Blatt, J. Catani, A. Celi, J. I. Cirac, M. Dalmonte, L. Fallani, K. Jansen, M. Lewenstein, S. Montangero, C. A. Muschik, B. Reznik, E. Rico, L. Tagliacozzo, K. Van Acoleyen, F. Verstraete, U.-J. Wiese, M. Wingate, J. Zakrzewski, and P. Zoller, Simulating lattice gauge theories within quantum technologies, *The European Physical Journal D* **74**, 165 (2020).
- [2] Y. Alexeev, D. Bacon, K. R. Brown, R. Calderbank, L. D. Carr, F. T. Chong, B. DeMarco, D. Englund, E. Farhi, B. Fefferman, A. V. Gorshkov, A. Houck, J. Kim, S. Kimmel, M. Lange, S. Lloyd, M. D. Lukin, D. Maslov, P. Maunz, C. Monroe, J. Preskill, M. Roetteler, M. J. Savage, and J. Thompson, Quantum computer systems for scientific discovery, *PRX Quantum* **2**, 017001 (2021).
- [3] C. Gatteringer and C. B. Lang, *Quantum chromodynamics on the lattice*, Vol. 788 (Springer, Berlin, 2010).
- [4] R. Pasechnik and M. Šumbera, Different faces of confinement, *Universe* **7**, 10.3390/universe7090330 (2021).
- [5] J. C. Halimeh, L. Homeier, H. Zhao, A. Bohrdt, F. Grusdt, P. Hauke, and J. Knolle, Enhancing disorder-free localization through dynamically emergent local symmetries (2021), [arXiv:2111.08715](https://arxiv.org/abs/2111.08715) [cond-mat.quant-gas].
- [6] A. S. Aramthottil, U. Bhattacharya, D. González-Cuadra, M. Lewenstein, L. Barbiero, and J. Zakrzewski, Scar states in deconfined  $\mathbb{Z}_2$  lattice gauge theories (2022), [arXiv:2201.10260](https://arxiv.org/abs/2201.10260) [quant-ph].
- [7] J. C. Halimeh and P. Hauke, Origin of staircase prethermalization in lattice gauge theories (2020), [arXiv:2004.07254](https://arxiv.org/abs/2004.07254) [cond-mat.str-el].
- [8] J. Berges, M. P. Heller, A. Mazeliauskas, and R. Venugopalan, Qcd thermalization: Ab initio approaches and interdisciplinary connections, *Rev. Mod. Phys.* **93**, 035003 (2021).
- [9] P. Hauke, F. M. Cucchietti, L. Tagliacozzo, I. Deutsch, and M. Lewenstein, Can one trust quantum simulators?, *Reports on Progress in Physics* **75**, 082401 (2012).
- [10] J. C. Halimeh, H. Lang, J. Mildnerberger, Z. Jiang, and P. Hauke, Gauge-symmetry protection using single-body terms, *PRX Quantum* **2**, 040311 (2021).
- [11] H. Lamm, S. Lawrence, and Y. Yamauchi, Suppressing coherent gauge drift in quantum simulations (2020), [arXiv:2005.12688](https://arxiv.org/abs/2005.12688) [quant-ph].
- [12] V. Kasper, T. V. Zache, F. Jendrzejewski, M. Lewenstein, and E. Zohar, Non-abelian gauge invariance from dynamical decoupling (2021), [arXiv:2012.08620](https://arxiv.org/abs/2012.08620) [quant-ph].

- [13] N. H. Nguyen, M. C. Tran, Y. Zhu, A. M. Green, C. H. Alderete, Z. Davoudi, and N. M. Linke, Digital quantum simulation of the schwinger model and symmetry protection with trapped ions (2021), [arXiv:2112.14262 \[quant-ph\]](#).
- [14] E. A. Martinez, C. A. Muschik, P. Schindler, D. Nigg, A. Erhard, M. Heyl, P. Hauke, M. Dalmonte, T. Monz, P. Zoller, and R. Blatt, Real-time dynamics of lattice gauge theories with a few-qubit quantum computer, *Nature* **534**, 516 (2016).
- [15] H. Bernien, S. Schwartz, A. Keesling, H. Levine, A. Omran, H. Pichler, S. Choi, A. S. Zibrov, M. Endres, M. Greiner, V. Vuletić, and M. D. Lukin, Probing many-body dynamics on a 51-atom quantum simulator, *Nature* **551**, 579 (2017).
- [16] A. Mil, T. V. Zache, A. Hegde, A. Xia, R. P. Bhatt, M. K. Oberthaler, P. Hauke, J. Berges, and F. Jendrzejewski, A scalable realization of local  $u(1)$  gauge invariance in cold atomic mixtures, *Science* **367**, 1128 (2020).
- [17] B. Yang, H. Sun, R. Ott, H.-Y. Wang, T. V. Zache, J. C. Halimeh, Z.-S. Yuan, P. Hauke, and J.-W. Pan, Observation of gauge invariance in a 71-site bose-hubbard quantum simulator, *Nature* **587**, 392 (2020).
- [18] N. Klco, E. F. Dumitrescu, A. J. McCaskey, T. D. Morris, R. C. Pooser, M. Sanz, E. Solano, P. Lougovski, and M. J. Savage, Quantum-classical computation of schwinger model dynamics using quantum computers, *Phys. Rev. A* **98**, 032331 (2018).
- [19] C. Schweizer, F. Grusdt, M. Berngruber, L. Barbiero, E. Demler, N. Goldman, I. Bloch, and M. Aidelsburger, Floquet approach to  $z_2$  lattice gauge theories with ultracold atoms in optical lattices, *Nature Physics* **15**, 1168 (2019).
- [20] Z. Wang, Z.-Y. Ge, Z. Xiang, X. Song, R.-Z. Huang, P. Song, X.-Y. Guo, L. Su, K. Xu, D. Zheng, and H. Fan, Observation of emergent  $\mathbb{Z}_2$  gauge invariance in a superconducting circuit (2021), [arXiv:2111.05048 \[quant-ph\]](#).
- [21] M. Heyl, P. Hauke, and P. Zoller, Quantum localization bounds trotter errors in digital quantum simulation, *Science Advances* **5**, eaau8342 (2019).
- [22] K. Chinni, M. H. Muñoz Arias, I. H. Deutsch, and P. M. Poggi, Trotter errors from dynamical structural instabilities of floquet maps in quantum simulation, *PRX Quantum* **3**, 010351 (2022).
- [23] V. Shende, S. Bullock, and I. Markov, Synthesis of quantum-logic circuits, *IEEE Transactions on Computer-Aided Design of Integrated Circuits and Systems* **25**, 1000 (2006).
- [24] J. C. Halimeh, H. Lang, and P. Hauke, Gauge protection in non-abelian lattice gauge theories (2021), [arXiv:2106.09032 \[cond-mat.quant-gas\]](#).
- [25] K. C. Young, M. Sarovar, and R. Blume-Kohout, Error suppression and error correction in adiabatic quantum computation: Techniques and challenges, *Phys. Rev. X* **3**, 041013 (2013).
- [26] K. S. C. Decker, C. Karrasch, J. Eisert, and D. M. Kennes, Floquet engineering topological many-body localized systems, *Phys. Rev. Lett.* **124**, 190601 (2020).
- [27] A. Smith, B. Jobst, A. G. Green, and F. Pollmann, Crossing a topological phase transition with a quantum computer (2021), [arXiv:1910.05351 \[cond-mat.str-el\]](#).
- [28] D.-W. Wang, C. Song, W. Feng, H. Cai, D. Xu, H. Deng, H. Li, D. Zheng, X. Zhu, H. Wang, S.-Y. Zhu, and M. O. Scully, Synthesis of antisymmetric spin exchange interaction and chiral spin clusters in superconducting circuits, *Nature Physics* **15**, 382 (2019).
- [29] P. Hauke, H. G. Katzgraber, W. Lechner, H. Nishimori, and W. D. Oliver, Perspectives of quantum annealing: methods and implementations, *Reports on Progress in Physics* **83**, 054401 (2020).
- [30] M. c. v. Kebrič, L. Barbiero, C. Reinmoser, U. Schollwöck, and F. Grusdt, Confinement and mott transitions of dynamical charges in one-dimensional lattice gauge theories, *Phys. Rev. Lett.* **127**, 167203 (2021).
- [31] J. C. Halimeh, V. Kasper, and P. Hauke, Fate of lattice gauge theories under decoherence (2020), [arXiv:2009.07848 \[cond-mat.quant-gas\]](#).
- [32] J. Schwinger, Gauge invariance and mass. ii, *Phys. Rev.* **128**, 2425 (1962).
- [33] J. Kogut and L. Susskind, Hamiltonian formulation of wilson's lattice gauge theories, *Phys. Rev. D* **11**, 395 (1975).
- [34] F. M. Surace, P. P. Mazza, G. Giudici, A. Leroose, A. Gambassi, and M. Dalmonte, Lattice gauge theories and string dynamics in rydberg atom quantum simulators, *Phys. Rev. X* **10**, 021041 (2020).
- [35] T. V. Zache, M. V. Damme, J. C. Halimeh, P. Hauke, and D. Banerjee, Achieving the continuum limit of quantum link lattice gauge theories on quantum devices (2021), [arXiv:2104.00025 \[hep-lat\]](#).
- [36] U.-J. Wiese, Ultracold quantum gases and lattice systems: quantum simulation of lattice gauge theories, *Annalen der Physik* **525**, 777 (2013).
- [37] F. Arute, K. Arya, R. Babbush, D. Bacon, J. C. Bardin, R. Barends, R. Biswas, S. Boixo, F. G. S. L. Brandao, D. A. Buell, B. Burkett, Y. Chen, Z. Chen, B. Chiaro, R. Collins, W. Courtney, A. Dunsworth, E. Farhi, B. Foxen, A. Fowler, C. Gidney, M. Giustina, R. Graff, K. Guerin, S. Habegger, M. P. Harrigan, M. J. Hartmann, A. Ho, M. Hoffmann, T. Huang, T. S. Humble, S. V. Isakov, E. Jeffrey, Z. Jiang, D. Kafri, K. Kechedzhi, J. Kelly, P. V. Klimov, S. Knysh, A. Korotkov, F. Kostritsa, D. Landhuis, M. Lindmark, E. Lucero, D. Lyakh, S. Mandrà, J. R. McClean, M. McEwen, A. Megrant, X. Mi, K. Michielsen, M. Mohseni, J. Mutus, O. Naaman, M. Neeley, C. Neill, M. Y. Niu, E. Ostby, A. Petukhov, J. C. Platt, C. Quintana, E. G. Rieffel, P. Roushan, N. C. Rubin, D. Sank, K. J. Satzinger, V. Smelyanskiy, K. J. Sung, M. D. Trevithick, A. Vainsencher, B. Villalonga, T. White, Z. J. Yao, P. Yeh, A. Zalcman, H. Neven, and J. M. Martinis, Quantum supremacy using a programmable superconducting processor, *Nature* **574**, 505 (2019).
- [38] F. Arute, K. Arya, R. Babbush, D. Bacon, J. C. Bardin, R. Barends, A. Bengtsson, S. Boixo, M. Broughton, B. B. Buckley, D. A. Buell, B. Burkett, N. Bushnell, Y. Chen, Z. Chen, Y.-A. Chen, B. Chiaro, R. Collins, S. J. Cotton, W. Courtney, S. Demura, A. Derk, A. Dunsworth, D. Eppens, T. Eickl, C. Erickson, E. Farhi, A. Fowler, B. Foxen, C. Gidney, M. Giustina, R. Graff, J. A. Gross, S. Habegger, M. P. Harrigan, A. Ho, S. Hong, T. Huang, W. Huggins, L. B. Ioffe, S. V. Isakov, E. Jeffrey, Z. Jiang, C. Jones, D. Kafri, K. Kechedzhi, J. Kelly, S. Kim, P. V. Klimov, A. N. Korotkov, F. Kostritsa, D. Landhuis, P. Laptev, M. Lindmark, E. Lucero, M. Marthaler, O. Martin, J. M. Martinis, A. Marusczyk,

- S. McArdle, J. R. McClean, T. McCourt, M. McEwen, A. Megrant, C. Mejuto-Zaera, X. Mi, M. Mohseni, W. Mruczkiewicz, J. Mutus, O. Naaman, M. Neeley, C. Neill, H. Neven, M. Newman, M. Y. Niu, T. E. O'Brien, E. Ostby, B. Pató, A. Petukhov, H. Putterman, C. Quintana, J.-M. Reiner, P. Roushan, N. C. Rubin, D. Sank, K. J. Satzinger, V. Smelyanskiy, D. Strain, K. J. Sung, P. Schmitteckert, M. Szalay, N. M. Tubman, A. Vainsencher, T. White, N. Vogt, Z. J. Yao, P. Yeh, A. Zalcman, and S. Zanker, Observation of separated dynamics of charge and spin in the fermi-hubbard model (2020), [arXiv:2010.07965 \[quant-ph\]](#).
- [39] L. M. Sieberer, T. Olsacher, A. Elben, M. Heyl, P. Hauke, F. Haake, and P. Zoller, Digital quantum simulation, trotter errors, and quantum chaos of the kicked top, [npj Quantum Information](#) **5**, 78 (2019).
- [40] C. Kargi, J. P. Dehollain, F. Henriques, L. M. Sieberer, T. Olsacher, P. Hauke, M. Heyl, P. Zoller, and N. K. Langford, Quantum chaos and trotterisation thresholds in digital quantum simulations (2021), [arXiv:2110.11113 \[quant-ph\]](#).
- [41] S. Lloyd, Universal quantum simulators, [Science](#) **273**, 1073 (1996).
- [42] K. Stannigel, P. Hauke, D. Marcos, M. Hafezi, S. Diehl, M. Dalmonte, and P. Zoller, Constrained dynamics via the zeno effect in quantum simulation: Implementing non-abelian lattice gauge theories with cold atoms, [Phys. Rev. Lett.](#) **112**, 120406 (2014).
- [43] E. Zohar and B. Reznik, Confinement and lattice quantum-electrodynamics electric flux tubes simulated with ultracold atoms, [Phys. Rev. Lett.](#) **107**, 275301 (2011).
- [44] D. Banerjee, M. Dalmonte, M. Müller, E. Rico, P. Stebler, U.-J. Wiese, and P. Zoller, Atomic quantum simulation of dynamical gauge fields coupled to fermionic matter: From string breaking to evolution after a quench, [Phys. Rev. Lett.](#) **109**, 175302 (2012).
- [45] E. Zohar, J. I. Cirac, and B. Reznik, Simulating  $(2 + 1)$ -dimensional lattice qed with dynamical matter using ultracold atoms, [Phys. Rev. Lett.](#) **110**, 055302 (2013).
- [46] O. Dutta, L. Tagliacozzo, M. Lewenstein, and J. Zakrzewski, Toolbox for abelian lattice gauge theories with synthetic matter, [Phys. Rev. A](#) **95**, 053608 (2017).
- [47] J. C. Halimeh and P. Hauke, Reliability of lattice gauge theories, [Phys. Rev. Lett.](#) **125**, 030503 (2020).
- [48] P. Facchi and S. Pascazio, Quantum zeno subspaces, [Phys. Rev. Lett.](#) **89**, 080401 (2002).
- [49] J. C. Halimeh, H. Zhao, P. Hauke, and J. Knolle, Stabilizing disorder-free localization (2022), [arXiv:2111.02427 \[cond-mat.dis-nn\]](#).
- [50] D. Abanin, W. De Roeck, W. W. Ho, and F. Huveneers, A rigorous theory of many-body prethermalization for periodically driven and closed quantum systems, [Communications in Mathematical Physics](#) **354**, 809 (2017).
- [51] M. V. Damme, H. Lang, P. Hauke, and J. C. Halimeh, Reliability of lattice gauge theories in the thermodynamic limit (2021), [arXiv:2104.07040 \[cond-mat.quant-gas\]](#).

## I. METHODS

### A. Target lattice gauge theories (LGTs)

#### 1. $\mathbb{Z}_2$ LGT

The  $\mathbb{Z}_2$  LGT in 1+1D considered in the main text is equivalent to the more common formulation with fermionic matter, described by the Hamiltonian [19, 30]

$$\begin{aligned} H_{\mathbb{Z}_2} = & J \sum_i \left( \psi_i^\dagger \tau_{i,i+1}^z \psi_{i+1} + \text{h.c.} \right) \\ & + f \sum_i \tau_{i,i+1}^x \\ & + \mu \sum_i (-1)^i \psi_i^\dagger \psi_i. \end{aligned} \quad (6)$$

Here,  $\psi_i^\dagger$  ( $\psi$ ) are fermionic creation (annihilation) operators and—compared to works such as Refs. [19, 30]—we have added a staggered fermion mass term  $\sim \mu$ . This term is compatible with the symmetries of the system and enables us to connect to the U(1) theory discussed below, where it is commonly included. Physically, it can be interpreted as giving a positive (negative) rest energy to (anti-)particles on even (odd) matter sites.

In the fermionic formulation of the  $\mathbb{Z}_2$  LGT, the symmetry generators are given by

$$G_i^{\mathbb{Z}_2} = e^{i\pi \psi_i^\dagger \psi_i} \prod_{i:\langle i,j \rangle} \tau_{i,j}^x. \quad (7)$$

Here,  $i : \langle i, j \rangle$  denotes the product over all links connected to matter site  $i$ . In our 1+1D case, these are  $\tau_{i,i-1}^x$  and  $\tau_{i,i+1}^x$ . Gauge symmetry is equivalent to  $[H_{\mathbb{Z}_2}, G_i^{\mathbb{Z}_2}] = 0 \forall i$ , and the conservation of the eigenvalues  $g_i^{\mathbb{Z}_2} = \pm 1$  of the generators,  $G_i^{\mathbb{Z}_2} |\psi(t)\rangle = g_i^{\mathbb{Z}_2} |\psi(t)\rangle \forall t$ .

The gauge violation respective to an initial, gauge-invariant state with eigenvalues  $g_i^{\text{in}}$  of the generators in Eq. (7) is quantified by

$$\eta_{\mathbb{Z}_2} = \frac{1}{N\kappa'} \sum_i \left\langle \left( G_i^{\mathbb{Z}_2} - g_i^{\text{in}} \right)^2 \right\rangle, \quad (8)$$

where  $\kappa'$  normalizes the maximal possible gauge violation to unity. This quantity can be understood as an average distance in Hilbert space from the target superselection sector defined by  $\{g_i^{\text{in}}\}$  [31], and non-zero values are equivalent to the presence of gauge errors.

Substituting the fermionic degrees of freedom by spins-1/2 via a Jordan–Wigner transformation,

$$\begin{aligned} \psi_i^\dagger &= e^{+i\pi \sum_{k<i} \sigma_k^+ \sigma_k^-} \sigma_i^+ \\ \psi_i &= e^{-i\pi \sum_{k<i} \sigma_k^+ \sigma_k^-} \sigma_i^-, \end{aligned} \quad (9)$$

which retains the canonical fermion anti-commutation relations, yields the Hamiltonian  $H$  and gauge generators reported in the main text.

#### 2. U(1) LGT

Consider the Kogut–Susskind Hamiltonian formulation of QED in 1+1D with staggered fermions [32, 33],

$$\begin{aligned} H^{\text{U}(1)} = & 2J \sum_i \left( \psi_i^\dagger U_{i,i+1} \psi_{i+1} + \text{h.c.} \right) \\ & + \mu \sum_i (-1)^i \psi_i^\dagger \psi_i + \frac{g^2}{2} \sum_i (E_{i,i+1} + E_0)^2, \end{aligned} \quad (10)$$

where the role of  $J$  and  $\mu$  is as in  $H_{\mathbb{Z}_2}$ . The last term gives the electric field energy and  $E_0$  is a background field, which in this theory is equivalent to a topological  $\theta$  angle [34, 35]. The electric field  $E_{i,i+1}$  and parallel transporters  $U_{j,j+1}$  fulfil the commutation relation

$$[E_{i,i+1}, U_{j,j+1}] = \delta_{ij} U_{i,i+1}. \quad (11)$$

This model has a continuous U(1) gauge symmetry with generators

$$G_i^{\text{U}(1)} = E_{i-1,i} - E_{i,i+1} + \psi_i^\dagger \psi_i + \frac{(-1)^i - 1}{2}. \quad (12)$$

We have  $[H^{\text{U}(1)}, G_i^{\text{U}(1)}] = 0 \forall i$ , and the eigenvalues  $g_i^{\text{U}(1)}$  of the generators,  $G_i^{\text{U}(1)} |\psi(t)\rangle = g_i^{\text{U}(1)} |\psi(t)\rangle$ , are conserved under Eq. (10).

The gauge fields can be expressed within the quantum link model formalism [36] with  $S = 1/2$  as  $U_{i,i+1} = \tau_{i,i+1}^+$ ,  $E_{i,i+1} = \frac{1}{2} \tau_{i,i+1}^z$ , which retains the system's symmetries and the commutation relation of Eq. (11). Again applying the Jordan–Wigner transformation as in Eq. (9) yields

$$\begin{aligned} H^{\text{U}(1)} = & 2J \sum_i \left( \sigma_i^+ \tau_{i,i+1}^+ \sigma_{i+1}^- + \text{h.c.} \right) \\ & + \frac{\mu}{2} \sum_i (-1)^i \sigma_i^z + \frac{E_0 g^2}{4} \sum_i \tau_{i,i+1}^z. \end{aligned} \quad (13)$$

Here, we employ  $(\tau_{i,i+1}^z)^2 = \mathbb{1}$  and neglect constant terms. Performing a basis rotation on the gauge fields such that  $\tau_{i,i+1}^x \leftrightarrow \tau_{i,i+1}^z$ ,  $\tau_{i,i+1}^y \rightarrow -\tau_{i,i+1}^y$ , thus  $\tau_{i,i+1}^+ \rightarrow (\tau_{i,i+1}^z - i\tau_{i,i+1}^y)/2$ , and redefining the constant  $E_0 g^2/4 \rightarrow f$  yields the U(1) gauge theory and generators reported in the main text.

The gauge violation respective to an initial, gauge-invariant state with eigenvalues  $g_i^{\text{in}}$  of the generators in Eq. (12) is quantified by

$$\eta_{\text{U}(1)} = \frac{1}{N\kappa} \sum_i \left\langle \left( G_i^{\text{U}(1)} - g_i^{\text{in}} \right)^2 \right\rangle, \quad (14)$$

with  $\kappa$  normalizing the maximal possible gauge violation to unity.



## B. Hardware

We implement the target LGTs in superconducting quantum chips of the Sycamore class, as have been described, e.g., in Refs. [37, 38]. The layout of these chips is that of a square lattice, which permits us to naturally map the qubits to the degrees of freedom of the 1+1D LGT by alternating assignment of matter sites and gauge links. More specifically, we employ the Rainbow and Weber chips, which host 23 and 53 qubits, respectively, of which we use up to 16 qubits under periodic and 21 qubits under open boundary conditions. The experiments were performed remotely via the cloud on devices that were calibrated using automated calibration procedures.

The Sycamore-class quantum chips natively implement arbitrary single qubit rotations around the  $z$  axis (which can be implemented virtually without execution time) and around arbitrary axes in the  $x$ - $y$  plane. The latter take a gate time of 25ns and their average error rate per gate is about 0.1%. In addition, these chips have a native two-qubit gate that approximates the form  $\exp(-i\frac{\theta}{2}(\sigma_1^x\sigma_2^x + \sigma_1^y\sigma_2^y)) \exp(-i\frac{\phi}{4}(\mathbb{1} - \sigma_1^z)(\mathbb{1} - \sigma_2^z))$ . Since  $\theta$  is close to  $\pi/4$  and  $\phi \simeq 0.138 \pm 0.015$  [38], this gate can to leading order be approximated as a  $\sqrt{\text{iSWAP}}^\dagger$  gate, with average error rates per gate of 1–1.5%. In some situations, though, the parasitic C-phase term  $\propto \phi$  can have considerable effects on the simulated dynamics. Indeed, in the scenario of, e.g., Fig. 3, we find its contribution to be the leading error term. A further relevant error term, not taken into account in our simulations, stems from readout, which is on the order of 2% ( $|0\rangle$ -state) to 7% ( $|1\rangle$ -state).

A more comprehensive description of the hardware used can be found in Ref. [37] and its Supplementary Material.

## C. Additional details on the quantum circuit

Since the single qubit rotations in Fig. 1b,c can be naturally realized in the Sycamore chip, the key implementation challenge is the decomposition of the matter–gauge coupling into single- and two-qubit gates. This decomposition can be realized as

$$\begin{aligned} U_{ijk}(\alpha) &= e^{-i\alpha(\sigma_i^+ \tau_j^z \sigma_k^- + \text{h.c.})} \\ &= e^{i\pi} \sqrt{\text{iS}}_{ij} \sqrt{\text{iS}}_{ij} R_i^z(\pi) R_j^z(-\pi/4) R_k^z(-\pi/4) \\ &\quad \sqrt{\text{iS}}_{jk} R_j^z(\pi - \alpha) R_k^z(\alpha) \sqrt{\text{iS}}_{jk} \\ &\quad R_j^z(\pi/4) R_k^z(\pi/4) \sqrt{\text{iS}}_{ij} \sqrt{\text{iS}}_{ij}, \end{aligned} \quad (15)$$

where  $i, k$  label qubits representing matter sites connected via qubit  $j$  representing the linking gauge field, and  $\sqrt{\text{iS}}_{ij}$  is denoting the square root of iSWAP gate ( $\sqrt{\text{iSWAP}}_{ij}$ ). It is useful to note that the latter is equal to the native  $\sqrt{\text{iS}}_{ij}^\dagger$  up to  $z$ -rotations as  $\sqrt{\text{iS}}_{ij}^\dagger = R_i^z(\pi/2) R_j^z(-\pi/2) \sqrt{\text{iS}}_{ij} R_i^z(-\pi/2) R_j^z(\pi/2)$ .

To limit decoherence, it is desirable to keep the execution time of the matter–gauge coupling as short as possible. Furthermore, idling qubits should be avoided as these are subject to erroneous  $z$ -rotations due to crosstalk and low-frequency noises. Hence, we compress the circuit by executing neighbouring gates in parallel wherever possible. Beyond this, we add spin echo sequences by randomly chosen angles on idling qubits.

A sketch of the full gate sequence can be found in Fig. 4.

## D. Use of large Trotter step sizes

In principle, we are interested in the simulation of the LGT dynamics in continuous time. As recent works have shown [21, 22, 39, 40], this does not require taking the limit of vanishing Trotter steps  $\Delta t \rightarrow 0$  in Eq. (2) as one might expect from worst-case bounds [41]. Instead, viewing the Trotterized dynamics as a periodic sequence of pulses, one can use techniques from periodically driven systems to identify a sharp crossover between regular and chaotic quantum dynamics. In the regular regime, the system dynamics deviates only perturbatively from the dynamics at  $\Delta t \rightarrow 0$ . Numerical benchmarks on finite systems show that the regular regime extends to surprisingly large Trotter step sizes and that its effect holds up to essentially infinite times [21, 22, 39, 40]. This enables a controlled simulation of continuous-time dynamics with large  $\Delta t$ .

In Fig. 5, we numerically investigate this effect for the  $\mathbb{Z}_2$  LGT considered here. Panel (a) displays the time evolution of the electric field  $\mathcal{E}$ , which quickly approaches the ideal, continuum-time curve ( $\mathcal{E}_0 = \lim_{\Delta t \rightarrow 0} \mathcal{E}$ ) as the Trotter step is diminished. Panel (b) displays the medium-time average of the deviation of the electric field, defined as  $\Delta \mathcal{E} = \frac{1}{m} \sum_{k=1}^m |\mathcal{E}_{\Delta t}(k\Delta t) - \mathcal{E}_0(k\Delta t)|$  with  $m = t_f/\Delta t$  the number of steps for the particular Trotter step size  $\Delta t$  and  $t_f = 10/J$  the final evolution time. At small  $\Delta t$ , the deviation increases only perturbatively as  $(\Delta t)^2$  (see also [21]). As this additional data shows, even large Trotter steps of  $\Delta t \approx 0.5/J$  and above lie in the perturbative, regular regime. In our quantum simulations, we use  $\Delta t \in \{0.2/J, 0.3/J\}$ , enabling us to reach significant simulation times  $t = n\Delta t$  at given number of Trotter steps  $n$  while keeping the Trotterization error at a controlled level.

## E. Qubit selection

For each studied scenario, we average over several configurations of qubits (chains or rings of given length) in order to reduce errors. Since the performance of qubits and gates varies in position as well as time, it is crucial to identify those that perform well in a given experimental session. While calibration data for readout, single-, and two-qubit gates can indicate qubits that per-

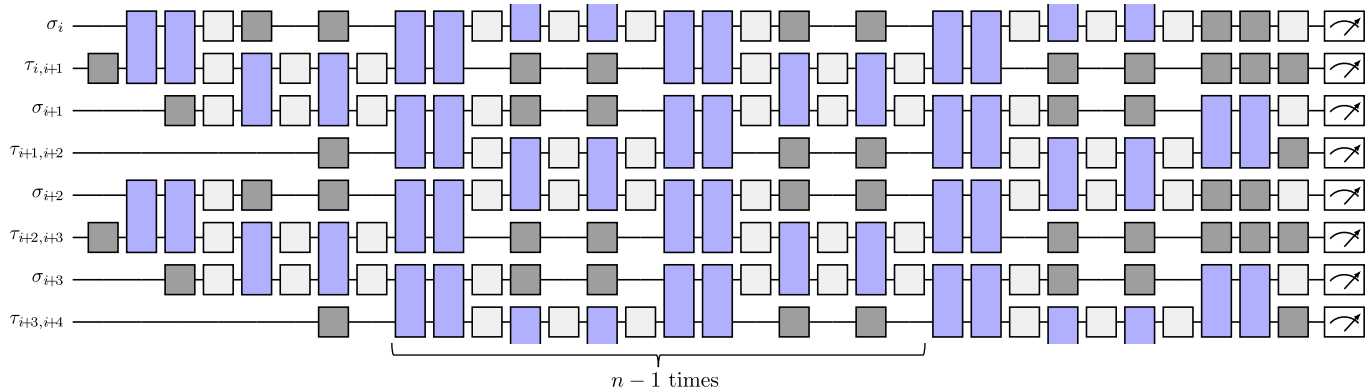


Figure 4. **Circuit diagram for  $n$  Trotter steps.** Two-qubit  $\sqrt{i}$ SWAP gates (blue) are executed in parallel to generalized single-qubit rotations (dark gray). Most of the latter arise from the purpose of avoiding idling qubits by acting as spin echo sequences, hence reducing errors induced by crosstalk with neighbouring, active qubits. Layers consisting only of  $z$ -rotations (light gray) require zero execution time. At the beginning of the circuit, it is beneficial to delay the initialisation of qubits as far as possible. Shown for an excerpt of eight qubits and the initial states of either Fig. 1a(ii) or (iii).

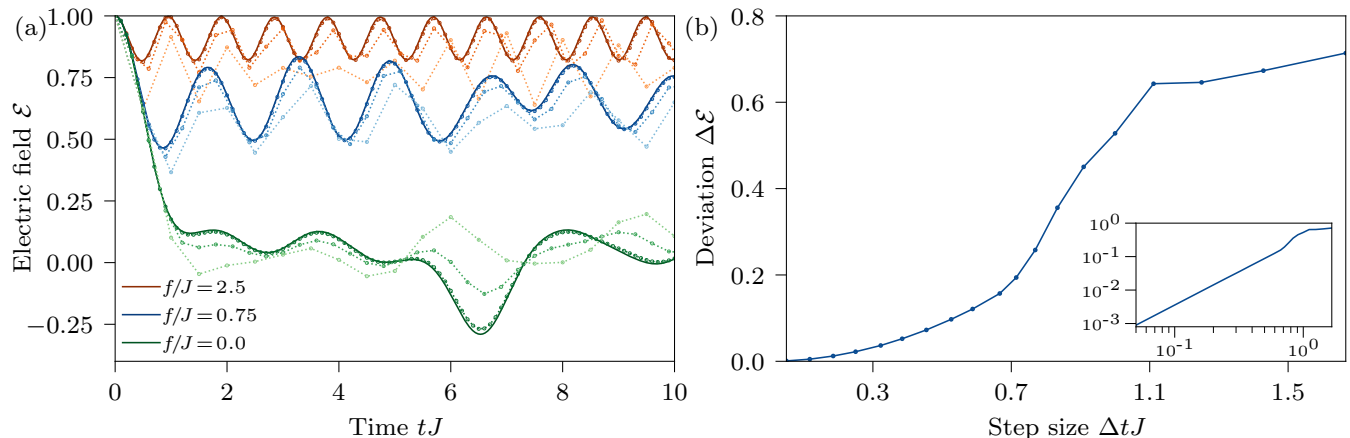


Figure 5. **Robustness of results against Trotter step size, numerical simulations.** (a) The range of Trotter step sizes used in our experiments introduce only small deviations of local observables from the continuum-time results (solid lines), illustrated here for the scenario of main-text Fig. 2, with step sizes  $0.1/J$ ,  $0.3/J$ ,  $0.5/J$ . (b) For small Trotter step sizes  $\Delta t$ , the deviation of the electric field from the time-continuum result increases quadratically until a sharp crossover from this perturbative to a chaotic regime around  $\Delta t \approx 0.7/J$ , see inset for log-log scale (example for the scenario of panel (a) with  $f/J = 0.75$ ). One can thus find an optimal balance of choosing  $\Delta t$  below the threshold, ensuring reliable results with controllable errors, while keeping it relatively large in order to reach significant evolution times at fixed number of Trotter steps (in our experiments, we use  $\Delta t \in \{0.2/J, 0.3/J\}$ ).

form especially bad, it does not pick out the best ensembles of qubits. Hence, we use a layered approach. At the beginning of a session, we use the calibration data to exclude the qubits and two-qubit gates identified to have particularly high error rates. In order to reduce the number of possible configurations (i.e., chains or rings for our purposes) to an amount feasible to benchmark, we further employ a simple cost function using the calibration data as input. We then use a minimal model for a specified parameter set to pick suitable ensembles among the remaining possible sets of qubits. To address time-dependent drifts within the duration of a session, we repeat the minimal model test between experiments, restricted to qubit sets performing well in the test at the

beginning of the session. With this procedure, we pick 5 chains of qubits in the case of Fig. 1d,e and 10 rings with periodic boundary conditions for Fig. 2 and Fig. 3, on which the experimental runs are executed and averaged over.

## F. Postselection

The local gauge symmetry also proves a useful tool to mitigate errors: any errors that break this local conservation law, akin to a stabilizer used in quantum error correction [25], can be identified through postselection.

This permits us to considerably improve the quality of the simulation.

As the implemented circuits respect the  $\mathbb{Z}_2$  gauge symmetry by design, any experimental shots where the eigenvalues of the generators Eq. (7) differ from those of the initial state are known not to be faithful. This is equivalent to the gauge-violation in Eq. (8) being non-zero. In addition, the total  $\mathbb{Z}_2$  charge  $\sum_i \sigma_i^z$  should ideally be conserved in our implementations, which we can use in postselection to further eliminate faulty experimental runs.

While total charge conservation is commonly used as a postselection criterion in quantum simulation (e.g., [13, 14, 38]), we find that the finer local conservation law provided by the gauge symmetry yields a significantly stronger improvement (see Extended Data Fig. 6). A potential reason is as follows. Two charge violation errors at separate sites, say  $i_1$  and  $i_2$ , can compensate each other to conserve the global charge. In contrast, they will be flagged by non-conservation of the Gauss' law generators  $G_{i_1}$  and  $G_{i_2}$ .

### G. Gauge-symmetry protection

Various methods have been developed in the past to restrain a quantum system to obey a desired symmetry, e.g., by engineered dephasing [42], by pseudo-random gauge transformations [11, 13], by dynamical decoupling [12], or by adding a suitable energy penalty to the Hamiltonian [10, 17, 43–47]. A particularly experimentally friendly approach is given by the concept of *linear gauge protection* [10], which entails adding to the Hamiltonian a term that is a linear weighted sum in the gauge-symmetry generators and that has a large strength  $V$ ,

$$H_G = V \sum_i c_i G_i^{U(1)}. \quad (16)$$

When the coefficients  $c_i$  are chosen appropriately, one can effectively turn the gauge superselection sectors (defined by the eigenvalues of the  $G_i^{U(1)}$ ) into quantum Zeno subspaces that remain uncoupled up to a timescale at least linear in  $V$  [48, 49].

Even more, when working in a single target gauge superselection sector, defined through the conserved charges  $\{g_i\} = \{g_i^{\text{tar}}\}$ , it suffices to only isolate this sector

from the rest of the Hilbert space. When the sequence  $c_i$  is *compliant*, i.e., it satisfies

$$\sum_i c_i (g_i - g_i^{\text{tar}}) = 0 \iff g_i = g_i^{\text{tar}}, \forall i, \quad (17)$$

the effective protection of the target gauge sector is guaranteed up to timescales exponential in the protection strength  $V$  [10, 50].

The relation (17) ensures that no combination of processes that violate the conservation of  $g_i^{\text{tar}}$  at different matter sites can be resonant. In principle, the sequence  $c_i$  will have to grow exponentially with system size in order to satisfy this relation. Interestingly though, depending on the dominant terms that couple the gauge superselection sectors, much simpler *noncompliant* sequences can already suffice to stabilize gauge invariance up to all relevant timescales [10, 51]. Extended Data Fig. 7 shows the results analogous to Fig. 3 of the main text for 16 qubits (8 matter sites, 8 gauge-field links) and the very simple sequence  $c_i = (-1)^i$ , which already suffices to produce satisfactory results. In the main text Fig. 3, we use the sequence  $c_i \in \{-115, 116, -118, 122, -130, 146\}/146$ , which is compliant for a system of  $N = 6$  matter sites. In larger systems, this sequence ensures that no combination of processes that violates conservation of  $G_i^{U(1)}$  is resonant within a distance of  $N = 6$  matter sites.

A main feature of Eq. (16) is that it involves only terms linear in the gauge-symmetry generators  $G_i^{U(1)}$ , enabling its implementation using only single-qubit terms. These incur no relevant experimental overhead in our implementation as they can be absorbed into already present terms.

A subtlety of the application of  $H_G$  comes from Trotterization [10]. In principle, one would want to make the associated scale  $V$  as large as possible in order to improve the level of U(1) gauge symmetry. However, in a Trotterized sequence the protection terms  $\exp(i\Delta t V c_i G_i^{U(1)})$  are periodic under  $\Delta t V c_i$ . Consequently, there is an optimal strength  $V^*$  beyond which protection no longer improves (conveniently for implementations, no fine tuning is required since a broad range of  $V$  around  $V^*$  yields comparable performance [10]). For our parameters,  $V^*$  is close to  $V/J = 6$ . Importantly, as seen in Fig. 3 we find that this moderate value already suffices to efficiently induce an approximate U(1) gauge symmetry.

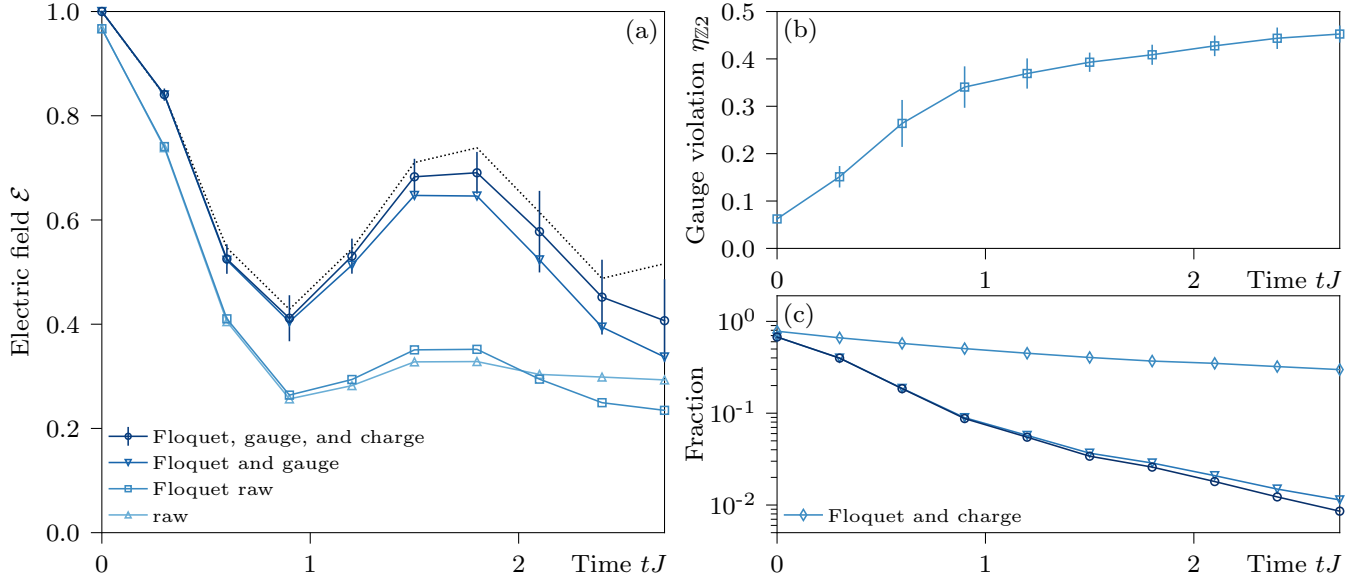


Figure 6. **Postselection and Floquet calibration.** (a) Raw data (lightest curve) display sizable discrepancies to the theoretical predictions (dotted). Floquet calibration yields slight improvements, while postselection on local  $\mathbb{Z}_2$  gauge symmetry significantly enhances the data quality. Postselection on global  $\mathbb{Z}_2$  charge results in a further small improvement. Data shown in the main text includes all these steps, illustrated here on data of Fig. 2 with  $f/J = 0.75$ . Statistical error bars denote one standard deviation over 10 different circuit layouts (shown only for one data set for clarity; error bars are of similar magnitude for other data sets). (b) Dynamics of  $\mathbb{Z}_2$  gauge violation of raw data with Floquet calibration. (c) Fraction of states fulfilling either of the two or both postselection criteria. The steeper decrease of the fraction of gauge-symmetric states illustrates that this is a stronger postselection criterion.

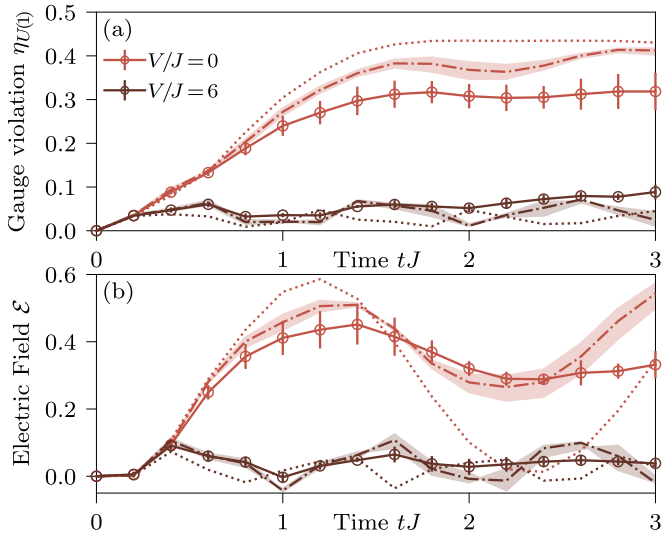


Figure 7. **Gauge protection and confinement induced by modified local conservation law with simple protection sequence.** The scenario is as in main-text Fig. 3, but for 16 qubits and the simple noncompliant sequence  $c_i = \pm 1$ , which nevertheless leads to satisfactory protection of  $U(1)$  gauge symmetry over the evolution time.